Evaluating the geochemistry and paired silicon and oxygen isotope record of quartz in siliceous rocks from the ~3 Ga Buhwa Greenstone Belt, Zimbabwe, a critical link to deciphering the Archean silica cycle

Latisha A. Brengman[2]*, Christopher M. Fedo[1], Martin J. Whitehouse[3], Iffat Jabeen[4], Neil R. Banerjee[4]

[1]Department of Earth and Planetary Sciences, University of Tennessee, Knoxville, TN 37996, USA, [2]Department of Earth and Environmental Sciences, University of Minnesota – Duluth, Duluth, MN, 55812 USA, [3]Department of Geosciences, Swedish Museum of Natural History, Stockholm, Sweden, SE-105 05, [4]Department of Earth Sciences, Western University, London, Ontario, Canada, N6A 5B7

Corresponding Author*: Latisha A. Brengman, Department of Earth and Environmental Sciences, University of Minnesota – Duluth, 1114 Kirby Drive, 221 Heller Hall, Duluth, MN, 55812, Phone: (218)-726-7586, Email: lbrengma@d.umn.edu

Keywords: silicon isotopes, oxygen isotopes, Mesoarchean silica cycle, Superior-type iron formation, Algoma-type iron formation, chert, geochemistry, source to sink

Outline

Abstract
1. Introduction
2. Geologic Context
   - *2.1. Lithologic assemblage, Structure and Metamorphism, Age constraints*
   - *2.2. Shelf association*
   - *2.3. Basinal association*
3. Analytical Methods
   - *3.1. Sample selection*
   - *3.2. Elemental geochemistry*
   - *3.3. Isotope geochemistry*
4. Petrography
5. Geochemistry results
   - *5.1. Major and trace element data*
   - *5.2. Silicon and oxygen isotope geochemistry results (IRMS)*
   - *5.3. Silicon isotope geochemistry results (SIMS)*
6. Tracking geochemical change from source-to-sink in the Buwha greenstone belt
   - *6.1. Multi-crystal geochemical and isotopic data from the Buhwa greenstone belt*
   - *6.2. Single-crystal isotope data - preservation potential of primary signatures?*
   - *6.3. Extreme isotope heterogeneity in siliceous precipitates – local or global?*
   - *6.4. A link to Archean weathering?*
7. Conclusions
8. References

Abstract

The balance of the Archean silica cycle links fundamentally to large scale processes that govern the composition of the ocean. Shifting contributions from continental or hydrothermal inputs of silica to the ocean is commonly recorded in silica-rich chemical precipitates. Such information is critical to interpreting primordial conditions in early life environments but reading the archive of silica-rich chemical sedimentary rocks remains challenging because of diagenetic and metamorphic overprinting. Here, we utilize a robust geochemical tool – silicon isotopes, to track silica from source to sink within a single Mesoarchean basin – the ~ 3 Ga Buhwa greenstone belt in Zimbabwe. We take a source to sink approach and measure the silicon isotope composition of source material, associated clastic rocks, and three different types of chemical sedimentary rocks (Superior-type iron formation, Algoma-type iron formation, and chert) from the same basin to investigate mechanisms for silicon isotope heterogeneity. We observe that iron formation and chert possess isotopically distinct values, similar to previous studies. Chert is commonly thought to preserve geochemical attributes of seawater; however, we find that silicon isotope values of chert samples vary widely even in a single basin. This could indicate that the water-column was not well-mixed, or that over short time scales within the Buhwa basin, the silica cycle was not in balance. Overall, data from the Buhwa greenstone belt suggest that basin-specific trends may convolute the compiled silicon isotope archive.

1. Introduction

Precambrian iron formation and chert form expansive chemical sedimentary deposits that preserve a range of depositional environments. The type and character of associated rocks also varies, dividing iron formation into distinct groups based on stratigraphic association and texture. Algoma-type iron formation and chert commonly interstratify with volcanic rocks and mineralogically immature clastic sedimentary rocks (e.g., Kimberley, 1979; Gross, 1980; Klein, 2005; Konhauser et al., 2017). By contrast, Superior-type iron formation typically intercalates with mineralogically mature sandstone and shale, and less commonly, carbonate (e.g., Kimberley, 1979; Gross, 1980; Klein, 2005; Konhauser et al., 2017). Texturally, iron formation divides into banded units that consist of mm-cm scale layers of alternating composition, and granular units, which consist of layers of potentially transported, sand- and mud-sized fragments. The compositional and textural differences along with differing lithologic associations make such classifications useful for considering geochemical processes responsible for influencing local compositional heterogeneity and sedimentary processes that may affect the preservation potential of a given chemical sedimentary unit. Because iron formation and associated chert potentially retain a record past seawater attributes (e.g., Knauth, 1994; Knauth and Lowe, 2003; Robert and Chaussidon, 2006; Konhauser et al., 2017), it is critical to make geochemical interpretations in the context of depositional processes and post-depositional alteration.

During the Archean (4 – 2.5 Ga; https://stratigraphy.org/timescale/) the relative balance between chemical weathering, tectonism, and volcanism contrasted from today given the expected evolution of the crust-ocean system over such a duration. The effects of this dynamic interplay on ocean composition can be investigated using geochemical and isotopic approaches applied to well-characterized suites of chemical sedimentary rocks, which provide an archive of the compositional evolution of Earth's oceans (e.g., Knauth, 1994; Knauth and Lowe, 2003; Robert and Chaussidon, 2006; Konhauser et al., 2017). The abundance of iron-oxide and quartz phases within iron formation (IF) has led to extensive research on the sources of iron and silicic

acid in IF and chert and include hydrothermal activity and chemical weathering of continental material. The precipitation of iron-rich phases iron in such deposits links indirectly or directly to biological activity via photosynthesis or photoferrotrophy, with contributions from dissimilatory iron reduction, and possibly aided by abiotic oxidation processes such as UV-photooxidation (e.g., Pecoits et al., 2015; Konhauser et al, 2017). Silicon, by contrast, is considered abiotic in origin because of the lack of genetic or fossil evidence for organisms that use biologic regulation to precipitate silica during the time frame of IF deposition (e.g., Siever, 1992), and at ~ 3 Ga certainly not within the timeframe of deposition of rocks studied here. With no known biological mechanism to remove silica, the early Precambrian ocean is considered to have reached silica-saturation (with estimated concentrations up to 2.2 mM for amorphous silica; Maliva et al., 2005). Evidence for such high silica concentrations could be reflected in the abundance of precipitated silica-rich layers in IF and bedded chert units.

Because the isotopes of silicon (^{28}Si, ^{29}Si, ^{30}Si) fractionate under a variety of abiotic conditions at Earth's surface, their ratios may be used to constrain mechanisms of quartz precipitation and develop a picture of the Precambrian silica cycle prior to the advent of biological utilization of silica. The homogenized silicon isotope value of the modern ocean reservoir ($\delta^{30}Si_{ocean}$ = +1.1 ‰; Ding et al., 1996; De la Rocha et al., 2000) is overwhelmingly buffered by the composition of silicic acid derived from chemical weathering of continental masses (^{30}Si-enriched) delivered to the ocean via major river systems and removed by silica utilizing organisms, such as diatoms, radiolarians, and siliceous sponges (Treguer and De la Rocha, 2013). Their remains produce the majority of silicic biogenic oozes that are ultimately preserved in the rock record as biogenic ("organic") bedded cherts (Boggs, 2001). Dissolution of chert deposits during burial supplies silica-rich fluids to more shallowly buried rocks for both cementation in pore spaces and mineral replacement. The balance between selective dissolution and reprecipitation (cementation) affects the isotope composition of pore fluids and associated secondary precipitates (Tatzel et al., 2015). Additionally, the presence of carrier phases (aluminum and iron) have a direct effect on isotopic composition and are associated with negative fractionation factors ($^{30}Si_{solid/solution}$) as much as -4.5 ‰ (Oelze et al., 2015) and ranging from -1.8 to -3.2 ‰ (Oelze et al., 2014).

The observed range of fractionation factors fundamentally links to the solid formation (precipitation) and adsorption rate. However, in systems or environments where the silica concentration of the fluid is near saturation, the silicon isotope composition of the precipitate can closely resemble the parent fluid (e.g., Ziegler et al., 2011; Tatzel et al., 2015). Such similarity between fluid and precipitate isotope composition provides evidence for a lack of fractionation during precipitation of chemically pure siliceous sedimentary rocks at times in Earth history when silica concentrations approached saturation. With this framework, we investigate iron-rich, iron-poor, and iron-free silica-rich rocks within a Mesoarchean basin to ascertain isotopic variation and its potential link to the silicon isotopic composition of seawater.

Silica-rich precipitates such as chert and iron formation serve not only as a compositional archive of past seawater, but also provide a direct view of the balance of a fundamental major element in the crust-ocean system. Silicon isotope compositions of siliceous rocks could link to relative proportions of continental versus hydrothermal contributions of this major element to Precambrian seawater (Heck et al., 2011) - a longstanding and critical question. Heterogeneity and preservation potential of isotopic signatures however limits the current ability to form a unified interpretation of the signatures preserved within the compiled silicon isotope archive. Previous studies attribute isotopic variation through time to a number of different factors -

including temperature variation, precipitation rate changes, adsorption, or clay authigenesis through time (Orpfergelt et al., 2009; Chakrabarti et al., 2012; Geilert et al., 2014; 2015; Oelze et al., 2014; 2015; Trower and Fischer, 2019). Part of this heterogeneity may relate to variation in the primary depositional environment, differential diagenetic histories, or local geochemical variation within single basins.

To investigate the potential silicon isotope link between different types of precipitates formed in separate parts of a single basin, we take a source-to-sink approach analyzing silicon isotope values of quartz from source material, clastic sedimentary rocks, and associated iron-rich and iron-poor and aluminum-poor silica-rich chemical sedimentary rocks from the ~3 Ga Buhwa greenstone belt, Zimbabwe. We use a multi-method approach, combining multi-mineral and single-crystal isotope analyses with major and trace element geochemistry to account for relationships to iron and aluminum.

2. Geologic Context

2.1 Lithologic assemblage, Structure and Metamorphism, Age constraints

Fedo et al. (1995), Fedo and Eriksson (1996), and Fedo et al. (1996) provided a comprehensive geologic history of the Buhwa greenstone belt (BGB). Here we highlight and summarize information critical to the present study. The Buhwa greenstone belt lies along the southern margin of the Zimbabwe craton along the margin with the Limpopo Belt (Figure 1), and approximately 30 km southeast of the well-studied Belingwe greenstone belt (Worst, 1962; Fedo and Eriksson, 1996). The main lithologic assemblage of the BGB consists of banded iron formation, chert, quartzite, phyllite, greenstone, and associated mafic intrusive rocks. Meta-sedimentary rocks divide into two main associations - a shelf association and a basinal association with a transitional unit between (Figure 2; Fedo and Eriksson, 1996). The ~3.5 - 3.2 Ga Tokwe segment (Fig. 3A) is an Archean crustal domain that forms the core of the Zimbabwe Craton and which crops out north of the BGB. Detrital zircon geochronology (Dodson et al., 1988) indicates the Tokwe segment represents at least part of the provenance region for silicicilastic meta-sedimentary rocks preserved in the BGB (Fedo et al., 1996). The tonalitic Chipinda tonalite forms a batholith (Fig. 1) emplaced at ~2.9 Ga that surrounds the northern margin of the BGB, and which locally contains quartzite xenoliths most likely derived from the BGB. The Chipinda tonalite is cross-cut by an east-trending mafic dyke that shares similarity to the regional Mashabi-Chibi dykes thought to represent feeder conduits to the ~2.7 Ga Ngezi Group mafic and ultramafic rocks (Wilson et al., 1987; 1990). Of interest within the BGB, this unit spreads along the Chipinda intrusive contact as a sill. Another unit, the ~2.6 Ga Chibi granite intrudes the Chipinda batholith (Figure 1; Hawkesworth et al., 1979; Fedo and Eriksson, 1996).

The BGB forms an east-plunging, open, asymmetric syncline through the shelf and transitional areas (Figure 1). Orthoquartzites preserve younging indicators including ripple marks and cross-bedding (Fedo and Erikkson, 1996; Figs. 2, 3B-F). Across-strike metamorphism notably increases from greenschist facies in the north to granulite facies in the south. Fine-grained tonalitic gneiss is common in the southern part of the belt where uplifted granulites crop out in the Northern Marginal zone of the Limpopo Belt. This event is dated at 2.58 - 2.71 Ga (Fedo and Eriksson, 1996). Along-strike metamorphism varies less dramatically from greenschist

in the west near the fold hinge to amphibolite facies in the east along the northern limb of the fold (Figure 1).

Age constraints from detrital zircon data and xenoliths in intrusives place the deposition of the BGB between ~2.9 and ~3.09 Ga (Fedo and Eriksson, 1996). Xenoliths of quartzite are present in the Chipinda batholith (~2.9 Ga), indicating a minimum age of deposition for the quartzite. Detrital zircons from the main BGB quartzite range provide a maximum age constraint of 3.09 ± 0.08 Ga, where zircons ages range from 3.09 ± 0.08 Ga to 3.81 ± 0.01 Ga (clustering at ~3.25 Ga; Dodson et al., 1988). Deformation associated with the Limpopo orogeny dates between ~2.7 and 2.6 Ga (e.g., Barton and van Reenen, 1992; Mkweli et al., 1995; Fedo and Eriksson, 1996). Previous studies observe no significant structural transport of lithologies.

2.2 Shelf association

The shelf association is best exposed near the fold hinge in the western part of the BGB (Figure 1). For simplicity, the following lithologic descriptions focus on protoliths and omit the prefix meta, though a degree of metamorphism is implied. Deformation fabrics are primarily expressed in the shale (now phyllite) as pressure solution cleavage and spaced cleavage, and at the base of the section at the contact with the Chipinda batholith.

There are five main lithologic units that comprise the shelf association: quartz arenite (quartzite, Q1), shale 1 (phyllite, S1), iron-formation (IF1), shale 2 (S2, phyllite), and greenstone (G1; Figure 2A). At the base of the section, the main lithologic units include interbedded quartzite and shale. Sedimentary structures are well-preserved in the upper part of the section and include cross-bedding, symmetrical ripple marks, mud drapes, and wavy and lenticular lamination (Figure 3B-F; Fedo and Eriksson, 1996). Overlying the main quartzite unit is a 1-km thick, dominantly shale unit (S1; Figure 2A). Millimeter-scale lamination, flame structures, wavy lamination, and symmetric ripples are present. Interbedded quartzite and a thick poorly sorted, matrix-supported conglomerate also occur within this predominantly shale unit (Figure 2A). Iron-formation intercalates with iron-rich laminated shales at the top of the section (Fedo et al., 1996). A thick succession of oxide facies iron formation (>500 m) overlies the shale (IF1l; Figure 2A; Figure 3G). Based on the classification scheme of Gross et al. (1980), this iron formation is classified as Superior-type, because of its direct association with sandstone and shale. Overlying the large iron formation unit, smaller hematite-rich, quartz-silt shale units interbed with thin iron formation units (S2). The succession is capped by very poorly exposed greenstone with thin interbeds of iron formation and quartzite or chert (G1; Figure 2A). Depositional environment interpretations are described fully in Fedo and Eriksson, 1996 and Fedo et al. (1996). Sedimentary structures and stacking patterns are consistent with a wave-swept shoreface to inner shelf environment in the lower part of the section that transitions to low-energy outer-shelf setting, followed by deposition of chemical sedimentary rocks.

A transitional area exists between the western shelf association and the eastern basinal association, where lithologies resembling each of the associations interfinger with each other. Shale (now phyllite) is the most common unit along with minor but distinct metaquartzites interpreted as recrystallized iron formation and chert (Figure 3H). Clastic units are hematite-rich and interlayer with iron-formation (Fedo and Eriksson, 1996). In the transitional area, of note, the iron formation divides into two distinct lithologies. One is along strike with the iron formation from the western shelf association, while the second closely resembles iron formation in the basinal association. Fedo and Eriksson (1996) interpret units within the transitional area to

represent basin-ward equivalents of the western shelf association with thin interbeds of the eastern basinal association. Quartzite units pinch out along the northern syncline limb, and the abundance of shale increases along strike. Interlayering of shale and iron formation that lack wave-induced sedimentary structures could indicate below-wave-base conditions. The different types of iron formation present in the BGB present the unique opportunity to directly compare iron formation attributes from potentially different sedimentation loci within the same basin.

2.3 Basinal association

The main basinal lithologies include greenstone, iron formation, and chert. Minor units include talc-tremolite and talc-dolomite schist, komatiite, mafic agglomerate, metaquartzite, and chlorite-quartz rocks. Metamorphic grade increases to the east, and locally in the basinal association; deformation obscures primary fabrics. Greenstone comprises the lowermost part of the stratigraphy (Figure 2B). Amphibole (dominantly tremolite) is common, and talc-tremolite, talc-dolomite schist occur towards the BGB core. Details are published in Fedo and Eriksson (1996). Areas that preserve primary fabrics include a mafic agglomerate, and spinifex and cumulate textures in komatiite, which preserve younging direction (Figure 2B). Iron formation (Figure 3I) in this association interlayers between greenstone and chert and could preserve soft sediment deformation features (Fedo et al., 1995). Because of the primary association with greenstone, the iron formation of the basinal association classifies as Algoma-type (Gross, 1980; Gorcerol et al., 2016). Chert (Figure 3J) varies from carbon-rich to mica-rich (namely muscovite, fuchsite, and biotite) and commonly intercalates with greenstone. Fedo and Eriksson, (1996) interpret the sedimentary units of basinal association to represent the deepest water deposits. Chemical sedimentary rocks could represent pelagic sedimentation linked to high silica concentrations in Mesoarchean seawater (Siever, 1992; Maliva et al., 2005) and the low influx of siliciclastic sediment. Intercalation with eruptive volcanic units could indicate a proximal source for iron and silica. Because there are three distinct iron formation lithologies within the BGB, we group samples according to their association and directly compare their petrographic and geochemical attributes.

3. Analytical methods

3.1 Sample selection

Superior-type IF, Algoma-type IF, chert, quartzite, and gneissic bedrock samples were carefully selected for geochemistry and isotope analyses; data are reported in Tables 1-4 and Supplementary Tables S1-S3. We measured major- and trace-element geochemistry from Tokwe segment bedrock gneiss (ZB 182), detrital quartz preserved in quartzite (ZB 240), three Superior-type iron formation samples (ZB 169, ZB 143, ZB 23) from the shelf association, three iron formation (ZB 17, 18, 20) and one chert (ZB 272) from the transitional area, and one Algoma-type iron formation (ZB 05), and three associated cherts (ZB 03, ZB 07, ZB 105) from the basinal association. Geochemical data is reported in Table 1, and Supplementary Table S1. We measured paired silicon ($\delta^{30}Si$) and oxygen ($\delta^{18}O$) isotope compositions of hand-separated quartz crystals from the same aliquot on nine of the iron formation and chert samples via isotope ratio mass spectrometry (IRMS) using methodology developed in the Laboratory for Stable Isotope Science at Western University (Hill et al., 2019). IRMS data is reported in Table 2, Supplementary Table S2. In addition, we measured single-crystal silicon isotope compositions of

quartz via Secondary Ion Mass Spectrometry (SIMS) using methodology developed by the NORDSIM facility at the Swedish Museum of Natural History. *In situ* isotopic analyses include quartz crystals from bedrock gneiss (n = 14), quartzite (n = 29), three Superior-type iron formation from the shelf association (n = 61), three iron formation (n = 60) and one chert (n = 20) from the transitional area, and one iron formation (n = 114), and three cherts (n = 103) from the basinal association. We report SIMS data in Table 3 and Supplementary Table S3.

3.2 Elemental Geochemistry

Rock samples collected from outcrops for major- and trace-element geochemistry were trimmed of weathering rinds, cut into ~1 cm pieces, and powdered in a SPEX shatterbox instrument using an alumina ceramic dish and puck. To clean the crushing surfaces between samples, we crushed massive, low-blank milky quartz. For major- and trace-element geochemical analyses, powdered whole-rock (multi-phase) samples were sent to Activation Laboratories Ltd. (Ancaster, Ontario). Samples were analyzed using a standard lithium metaborate/tetraborate fusion process for a suite of 46 elements, prepared in a standard batch system (with a method reagent blank, certified reference material, and 17% replicates; Protocol 4Lithores – Lithium Metaborate/Tetraborate fusion). Inductively coupled plasma optical emission spectrometry (ICP-OES) was used to measure major oxides and select trace elements (Ba, Sr), using either a combination simultaneous/sequential Thermo Jarrell-Ash ENVIRO II ICP or a Varian Vista 735 IC. Inductively coupled plasma mass spectrometry (ICP-MS) was used to measure all other trace elements on either a Perkin Elmer Sciex ELAN 6000, 6100 or 9000 ICP-MS instrument. USGS and CANMET certified reference materials (DNC-1, GBW 07113, LKSD-3, W-2a, SY-4, CTA-AC-1, BIR-1a, NCS DC86312, NCS DC70014, NCS DC70009, OREAS 100a, OREAS101a, JR-1) were used for comparison to all unknowns. Three blanks and five controls were analyzed per sample group. Duplicates were inserted every 15 samples, and the instrument was recalibrated after every 40 samples. Reproducibility (within 5%) was determined based on multiple analyses of randomly selected samples across different analytical sessions. We report detection limits for all elements in Tables 1, and S1.

3.3 Isotope Geochemistry

Prentice et al. (2014), Hill et al. (2019) and Brengman et al. (in press) outline methods for silicon and oxygen isotope measurements of a single, 1 mg aliquot using a fluorination-IRMS. Replicate analyses of international standard NBS-28 have a precision of 0.06‰ for $\delta^{29}Si$ and 0.04‰ for $\delta^{30}Si$. We report all silicon isotope values compared to NBS-28 (Equation 1).

Equation 1. $\delta^{30}Si=[(^{30}Si/^{28}Si_{sample})/ (^{30}Si/^{28}Si_{standard})–1]x1000.$

We report oxygen isotope data compared to international standard V-SMOW (Equation 2).

Equation 2. $(\delta^{18}O=[(^{18}O/^{16}O_{sample})/ (^{18}O/^{16}O_{standard})–1]x1000.$

Sample preparation and analytical details for SIMS analyses are reported in Brengman et al. (in press). We embedded small rock chips and/or cut thin sections) in epoxy along with a silicon isotope quartz reference material (NBS-28, and internal standard UTQ; Table S3). Mounts were polished, mapped, and gold-coated (30 nm) prior to analysis. *In situ* Si-isotope ($^{30}Si/^{28}Si$) measurements were made at the Swedish Museum of Natural History, Stockholm (NordSIMS facility) using a CAMECA IMS 1280 SIMS. Analytical conditions were as follows: $^{133}Cs+$ primary beam (ca. 5nA), incident energy of 20 keV. Reference materials were analyzed

in regularly bracketed intervals after every ten unknowns. Pre-sputter was used to remove the gold coating, followed by beam centered and 48 seconds of data acquisition. We report all isotope data using standard isotope notation (Equations 1 and 2 above). Instrumental mass fractionation was corrected using internal standard UTQ with a multi-crystal δ^{30}Si value of 0.08 ± 0.01 ‰, determined at Western University by fluorination IRMS. External reproducibility (1σ) for δ^{30}Si of ± 0.15 ‰ was derived from the bracketing of analyses and propagated onto within-run uncertainties. We applied a general correction factor to account for difference between the isotopic composition of the internal standard compared to the international standard (NBS-28). All silicon isotope data obtained via SIMS are reported in Table 3 (summary) and Table S3. For clarity and comparison to IRMS data, we use probability density functions (c.f., Marin-Carbonne et al., 2012) to describe *in situ* data (Table 3). Equations are as follows:

Equation 4: $$f_{\delta^{30}Si,\sigma}(x) = \frac{1}{\sigma \times \sqrt{2\pi}} \times \exp\left[\frac{-(x-\delta^{30}Si)^2}{2\sigma^2}\right]$$

Equation 5: $$P(x) = \int_{-\infty}^{+\infty} F(x) \times dx = 1 \text{ with } F(x) = \sum_{j=1}^{j=N} \frac{f\delta^{30}Si_{j,\sigma_j}(x)}{N}$$

Equation 6 (error): $$max\big(F(x)\big) - min\left(\frac{F(x)-\max(F(x))}{2}\right)$$

We report these results in Table 3.

4. Petrography

We examined 25 samples of chemical sedimentary rocks from the shelf, transitional and basinal associations and report their textural and mineralogical attributes here. We provide descriptions of associated clastic sedimentary rocks of the shelf association for context. Additional details for associated samples from the BGB exist in Fedo et al. (1995), Fedo et al. (1996), Fedo and Eriksson (1996). The basal quartzite unit of the shelf association is mineralogically mature, classifying as a quartz arenite (Figure 4A). Clasts are well-rounded, ranging in size from fine-to-medium sand. Quartz cement fills space between grains. Shale (now phyllite) consists of varying proportions of quartz silt (Figure 4B, C), and contains a dominant mineral assemblage of quartz, sericite, and chlorite (Figure 4C). Chemically, these shales are also mature, interpreted to reflect extreme chemical weathering of the source terrane (Fedo et al., 1996). Overall, the shelf association contains no feldspar or mineralogically immature clastic rocks. Superior-type iron formation of the shelf association contains quartz, hematite, and magnetite (Figure 4D). Within the basinal association, iron formation does not contain hematite, and instead primarily consists of quartz, magnetite, and minor amounts of amphibole (Figure 4E). Associated chert contains varying proportions of organic material (now graphite; Figure 4F), and fuchsite. Crystal size varies between samples, ranging from micro-quartz to mega-quartz. Shelf association samples are dominantly finer-grained (containing micro-quartz).

5. Geochemistry results

5.1 Major- and trace-element data

We measured major- and trace-element composition of chemical sedimentary rocks (chert, iron formation) from the shelf association (3 samples), the basinal association (4

samples), and the transitional area between the two (4 samples). Seven of the samples classify as iron formation based on iron content, the remaining samples classify as chert, though some have minor amounts of iron, organic material, and fuchsite. From the shelf association, iron formation samples range in total iron content from 34.8 - 64.9 wt. %, and from 34.1 - 63.1 wt. % in SiO_2 content (samples ZB 169, ZB 143, and ZB 23). All other elements show minor variation <0.1 wt. %, except for aluminum, which ranges from 0.3 - 0.6 wt. %. Transitional iron formation samples (ZB 17, ZB 18, ZB 20) have higher SiO_2 contents and lower total iron content, ranging from 61.9 - 79.2 wt. % (SiO_2) and 17.1 - 30.3 wt. % (FeOT). Chert from the transitional area (ZB 272) has slightly higher silica content, and less iron (93.5 wt. % SiO_2; 5.4 wt. % FeOT). Iron formation from the basinal association contains 49.6 wt. % SiO_2, and 47.0 wt. % FeOT, while associated chert ranges in SiO_2 content from 97.5 - 99.7 wt. % and iron content from 0.1 to 1.3 wt. % (FeOT). Aluminum contents in all samples are relatively low and show no systematic differences between the associations. Values range from 0.2 - 0.8 wt. %, except for the fuchsitic chert sample ZB 07 which contains 2.0 wt. % Al_2O_3. A few samples show minor amounts of major elements (magnesium, calcium, and potassium) that link to the presence of accessory phases (Table 1). Because of the potential for fractionation of silicon isotopes linked to the presence of iron and aluminum, we discuss iron, aluminum, and silicon content later in concert with isotopic data for the sample samples.

Trace-element compositions show minor variation between associations. Traditional rare earth element attributes of seawater (positive lanthanum anomalies, anomalous yttrium behavior, and an overall positive slope, Bolhar et al., 2004) are consistent across the shelf and basinal associations. In all samples, La/La* values are > 1, Y/Ho values ranging from 28.2 - 44.4, and Pr/Yb values are < 1 (Figure 5; Table 1). Fedo et al. (1996) performed a comprehensive analysis of associated iron-rich shales from the BGB, and we plot shale data from each association for context (Figure 5). All iron-rich samples possess europium anomalies (Eu/Eu* = 1.8 - 2.8), potentially indicating a role for hydrothermal fluids. Because of the degree of surface weathering and exposure of surface outcrops, we do not consider the anomalous behavior of cerium to indicate depositional conditions in relation to oxygen. Instead, cerium behavior observed here likely reflects surface alteration and oxidation in outcrop. There is no systematic change in the Ge/Si ratios for the shelf-to-basin transition; however, we do observe a direct correlation of Ge with iron content and Eu/Eu* anomaly (Figure 6A, B). This may indicate the association of Ge with iron-rich phases in the sample set.

5.2 Silicon and oxygen isotope geochemistry results (IRMS)

To directly investigate silicon isotope variations in one system from shelf to basin, we measured silicon and oxygen isotope values of chert and iron formation from the shelf, transitional, and basinal associations in the BGB. Silicon isotope values ($\delta^{30}Si_{NBS\text{-}28}$) range from -2.5 to -0.5 ‰ (1σ = 0.03 ‰) in iron-formation samples, and -1.1 to -0.50 ‰ (1σ = 0.03 ‰) in chert samples (Figure 7A, B). Samples show a broad, weak correlation with Ge/Si content and silicon isotope values (Figure 7A), though there are many possible interpretations for the apparent visual co-variation. Oxygen isotope values ($\delta^{18}O_{V\text{-}SMOW}$) range from 9.41 to 15.10 ‰ (1σ = 0.03 ‰; Figure 7B). We report $\delta^{29}Si$ and $\delta^{17}O$ values in Table 2. Compared to other Archean cherts, all samples from the BGB have ^{30}Si-depleted signatures (Figure 7B). There are no systematic trends or differences between shelf and basinal association samples. Chert samples (circles; Figure 7) possess ^{30}Si-enriched and ^{18}O-enriched isotopic signatures compared to iron-

rich samples (squares; Figure 7). Silicon isotope values generally decrease with increasing iron content (Figure 8A) and europium anomaly (Eu/Eu*) and show no correlation with aluminum content (Figure 8B). Compared to other Mesoarchean iron formation samples (Delvinge et al., 2012; Geilert et al., 2014), BGB samples show generally ^{30}Si-depleted values and less aluminum content (Figure 8). Silicon isotope values are broadly comparable to those measured in Delvinge et al., (2012).

5.3 Silicon isotope geochemistry results (SIMS)

To address quartz-specific isotopic variation within single samples, we measured silicon isotope values of individual quartz crystals using SIMS. We targeted quartz from >3 Ga Tokwe gneiss (ZB 182; representative continental bedrock upon which the succession was deposited), a quartz-cemented quartz arenite (ZB 240; containing quartz derived from weathering and transport of continental material), Superior-type BIF (ZB 17, 18, 20, 23, 143, 169), Algoma-type BIF (ZB 05), and interbedded recrystallized chert (ZB 03, 07, 105). Quartz crystals from a gneissic bedrock sample (Tokwe segment; Dodson et al., 1988; Wilson, 1990; ZB 182) possess an overall δ^{30}Si signature near ~+1 ‰, with comparatively little internal heterogeneity (δ^{30}Si = +0.5 ± 0.4 to +1.5 ± 0.4 ‰, Figure 9A, B). Individual monocrystalline quartz grains from a weakly metamorphosed quartz arenite sample from the BGB, with quartz sand likely derived from the Tokwe segment (Fedo and Eriksson, 1996), possess a similar, relatively homogeneous δ^{30}Si signature near ~+1 ‰, (δ^{30}Si = -0.2 ± 0.4 to +1.2 ± 0.4 ‰; Fig. 9; Tables 3, S3). Overall, chert and iron formation samples range from δ^{30}Si = -4.3 ± 0.3 to +1.6 ± 0.3 ‰ and show increased inter- and intra-sample heterogeneity relative to gneissic bedrock and quartzite (sandstone; Figure 9A, B; Tables 3; S3). Sub-divided, thin units of iron formation from the transitional area interbedded with shale range from δ^{30}Si = -2.1 ± 0.4 ‰ to -0.2 ± 0.3 ‰ (Figure 9A, B; Tables 3, S3); samples from the thicker unit of Superior-type iron formation of the shelf association range from δ^{30}Si = -3.3 ± 0.7 ‰ to -0.3 ± 0.4 ‰ (Figure 9A, B; Tables 3, S3). Thin units of iron-poor chert interbedded with shale in the transitional area range from δ^{30}Si = -4.3 ± 0.3 ‰ to -2.5 ± 0.2 ‰ (Fig. 9; Tables 3, S3). Algoma-type iron formation interbedded with altered volcanic rocks from the basinal association range from δ^{30}Si = -3.8 ± 0.2 ‰ to -1.0 ± 0.3 ‰ (Figure 9A, B; Tables 3, S3). Silicon isotope values of chert interbedded with altered volcanic rocks in the basinal association range from δ^{30}Si = -2.8 ± 0.2 ‰ to +1.6 ± 0.3 ‰ (Figure 9A, B; Tables 3, S3). All δ^{30}Si values for quartz within iron formation are less than 0 ‰, while about one-half of δ^{30}Si values for chert plot greater than 0 ‰. There are no systematic inter- or intra-sample trends; instead, single bands may contain the entire range of values measured in a single sample.

6. Tracking geochemical change from source-to-sink in the Buwha greenstone belt

Within the BGB, we can directly track geochemical and isotopic compositions of different types of silica sinks - Superior-type iron formation, Algoma-type iron formation, and chert. Sources of material to the basin can be estimated based on shale geochemistry and sandstone petrogenesis. Fedo et al. (1996) reported shale geochemistry for samples of the shelf, transitional, and basinal associations of the BGB. Overall, they determined that shale geochemistry indicates clastic sediment was sourced from the tonalite, granite, and mafic volcanics common in the Zimbabwe Craton. The early Archean (~3.09 - 3.5 Ga) Tokwe gneiss

(tonalite composition), is a good compositional candidate for the majority of clastic material to the basin. In the following text, we discuss the Buhwa depositional system in terms of sources and sinks for the basin-specific silica cycling. Because both chert and IF accumulated in a shelf association and basinal association, where different silica sources might dominate, we postulate these different rocks could record distinct isotopic and geochemical signatures related to the silica source, and composition of the reservoir from which each precipitated.

6.1 Multi-crystal geochemical and isotopic data from the Buhwa greenstone belt

Shale normalized trace element geochemical characteristics of Archean seawater precipitates such as chert and iron formation include: (1) positive lanthanum anomalies ($La/La^*_{SN} > 1$), (2) positive yttrium anomalies (associated with super-chondritic Y/Ho ratios), (3) light and middle rare-earth-element depletion compared to heavy rare-earth-elements ($Pr/Yb_{SN} < 1$; e.g., Bolhar et al., 2004). Additionally, many Archean samples possess a europium anomaly (Eu/Eu^*_{SN}), linked to the reduction of Eu^{3+} during fluid rock interaction at high temperatures (Michard et al., 1986; Danielson et al., 1992). Most chert and iron formation samples from the BGB possess positive lanthanum anomalies (Table 1; $La/La^*_{SN} = 1.05$ to 1.57, excluding 1 sample (ZB 20) $La/La^*_{SN} = 0.75$), and positive europium anomalies (Table 1; $Eu/Eu^*_{SN} = 1.05 – 2.84$; excluding 1 sample (ZB 07) $Eu/Eu^*_{SN} = 0.88$). While evidence for clastic contamination is minimal (Table 1; Al_2O_3 and Zr contents), some samples possess Y/Ho values that resemble crustal signatures and fall below the expected super-chondritic range for chemical sedimentary rocks (Table 1; Y/Ho = 28 – 44). Iron formation samples from the shelf association broadly possess lower Y/Ho signatures compared to iron formation from the transitional and basinal association (Table 1). It is therefore possible that shelf samples preserve geochemical signatures linked to continentally derived source material, though it should be noted that there is no clear systematic shelf to basin clastic contamination trend in aluminum or zirconium contents of the same samples.

Previous studies have utilized the ratio of Ge/Si to examine the relative contributions between continental and hydrothermal inputs in iron-rich chemical sedimentary rocks (e.g., Delvinge et al., 2012). Ge/Si ratios of Fe-rich bands in iron formation are interpreted to indicate inheritance from hydrothermal signatures, in contrast to low Ge/Si ratios measured in silica-rich bands (Hamade et al., 2003; Frei and Polat, 2007). Within BGB samples, we observe a weak correlation with iron content (Figure 6A; which also correlates with the europium anomaly; Figure 6B), though we did not separate out individual bands for whole rock geochemical analyses. Paired with silicon isotopes, Ge/Si ratios overlap with previously measured values of Archean iron formation (e.g., Delvigne et al., 2012). Though samples appear to show a weak correlation between the two measurements (Figure 7A), Ge/Si ratios appear to closely track iron contents, which may also account for the isotopic depletion (Figure 6A). Paired silicon and oxygen isotope analysis of quartz separates via IRMS (Figure 7B) reveal isotopic differences between iron-rich (squares) and iron-poor (circles) samples in both silicon and oxygen. Iron-rich samples (dark blue squares) have lower oxygen isotope values than iron-poor samples (dark blue circles) from the same association (basinal). This could indicate the presence of an iron phase such as magnetite or hematite as inclusions in quartz, which would result in lower oxygen isotope values (e.g., Perry et al., 1973). Alternatively, incomplete separation could have left behind minor amounts of iron-oxides which would result in iron-rich samples having lower oxygen isotope values.

Similar to other studies of Archean iron formation and cherts (e.g., Robert and Chaussidon, 2006; Marin-Carbonne et al., 2012), iron-rich samples possess ^{30}Si-depleted silicon isotope signatures (Figure 8A). Silicon isotope values and iron contents for samples from the BGB overlap with data from previous studies of comparable Archean samples (e.g., Delvinge et al., 2012; Geilert et al., 2014). Chert and iron formation samples from the BGB do not fall within the expected range of silicon isotope values or aluminum contents (Figure 8B) for silicified rocks based on previous work by Marin-Carbonne et al. (2012), and so likely represent true chemical sedimentary units. Textural data from thin section also confirms that samples are not likely silicified (see section 4). Overall, isotopically light (^{30}Si-depleted) silicon isotope signatures for BGB chert and iron formation samples may indicate precipitation from a reservoir influenced by hydrothermal fluids (Figure 8B). The presence of europium anomalies and high Ge/Si values in some samples, may provide additional support for such an interpretation. We explore potential mechanisms of fractionation and reasons for isotopic heterogeneity between samples in the next section in combination with single crystal data obtained from SIMS in the next sections. To compare the two different types of data (multi versus single crystal), we calculated probability density functions for *in situ* single crystal data for each sample (Table 3). Except for two organic carbon-rich samples (discussed in the next sections), all whole rock (multi-crystal) isotopic data plots within error of the peak value for the distribution of data for individual, single crystal analyses.

6.2 Single-crystal isotope data - preservation potential of primary signatures?

Collectively, silicon isotope values of siliceous precipitates from the BGB basin span nearly the entire known isotopic range for terrestrial rocks (~δ^{30}Si ~ 6 per mil, Figure 9A). Previous studies confirm the preservation potential of silicon isotopes through amphibolite facies metamorphic conditions (André et al., 2006; Brengman, 2015; Brengman et al., 2016). In the BGB, we find no systematic correlation between crystal size variation and isotope values (Brengman, 2015). Comparable silicon isotope values from quartz in the quartzite and quartz in the Tokwe segment may be another line of evidence against metamorphic resetting. Quartz from the quartzite derives from the Tokwe segment based on previous work by Fedo et al. (1996). The overlap in silicon isotope values between bedrock gneiss (ZB 182) and derived detrital quartz sand in quartzite (sandstone; ZB 240; Figure 9A) is consistent with the lack of a mechanism to fractionate silicon isotopes during the mechanical breakdown (and subsequent transport and deposition) of quartz in the source. Additionally, the BGB shelf rocks were metamorphosed to greenschist facies and recrystallized post deposition. Despite this metamorphism, source bedrock quartz still overlaps in composition with quartz in the quartzite. Therefore, it is possible that the BGB inter- and intra-isotope heterogeneity is primary or links to early diagenetic processes, similar to the conclusion drawn by Stefurak et al. (2015) in the Barberton greenstone belt. If such heterogeneity is primary, then it could indicate that silicon isotope compositions preserved in chemical sedimentary rocks from the BGB do not link to a widespread, well-mixed, water column representative of ocean composition, but point to processes acting at a more local scale.

6.3 Extreme isotope heterogeneity in siliceous precipitates – local or global?

Combining measured silicon isotope source values with estimated isotope values for dissolved silicon values provides a framework for investigating the fractionation mechanisms

responsible for the large degree of isotopic heterogeneity measured within rocks that represent silicon sinks within the BGB. Silicon isotope values of quartz from samples of chert and IF display a greater degree of intra- and inter-sample heterogeneity than associated bedrock and sandstone samples (Figure 9 A, B). Silicon isotope fractionation occurs during precipitation due to changing precipitation rates under varying geochemical and system conditions (open-to-closed) ($^{30}Si_{precipitate\text{-}solution}$ > 5 ‰ Oelze et al., 2014; 2015; $^{30}Si_{precipitate\text{-}solution}$ > 2.5 ‰; Delstanche et al., 2009; Opfergelt et al., 2010). When the rate of quartz precipitation is rapid, a larger difference is observed between the ^{30}Si composition of the solid phase and the fluid from which it precipitated, suggesting the operation of a kinetic isotope effect (Zheng et al., 2019). The magnitude of that fractionation can vary significantly, particularly with the addition of Al or Fe in the system. Samples from other Archean localities share similar isotopic trends to BGB samples with respect to iron and aluminum content (Figure 8A; Geilert et al., 2014; Delvinge et al., 2012). Aluminum is only prevalent in one chert sample from this study, and so cannot be responsible for all isotopic variation measured within chert samples (Table 1). Two samples - ZB 03 and ZB 105 contain minor amounts of organic material in the form of black chert layers that alternate with white chert layers. Recent work (Stamm et al., 2020) suggests a potential link between organic material and negative fractionation factors, but this link remains to be demonstrated conclusively in the rock record. Given this behavior, we interpret the wide range of silicon isotope values for any segregate group of samples in the BGB (Figure 9A, B; Tables 3; S3) to result from differences in the magnitude of kinetic isotope effects because of Al/Fe adsorption, combined with potentially changing quartz precipitation rates (Oelze et al., 2015; Figure 8A, 8B).

Silicon isotope values of pure siliceous precipitates (chert) are thought to most closely approximate seawater composition when silica concentrations are high (e.g., Ziegler et al., 2011; Tatzel et al., 2015). However, within the BGB, even silicon isotope compositions of chert (iron-poor samples) from the transitional and basinal associations vary widely (Figure 9A, B), and maximum measured isotope compositions do not always overlap. This could indicate isotopic heterogeneity within the basin over the time intervals of deposition. Heterogeneity could be primary - linked to differences in isotopic composition of primary source fluids (hydrothermal versus continentally derived silicic acid), or it could reflect changing reservoir composition over short timescales. Such short-term changes in reservoir composition could link to precipitation of vast amounts of ^{30}Si-depleted silica precipitated in associated iron formation, leading to isotopic enrichment of the reservoir, indicating short term variation in basinal silica concentrations.

6.4 A link to Archean weathering?

While the relative balance between continental and hydrothermal silica and silicic acid washed into the ocean from the continents has varied over Earth history (Allègre and Rousseau, 1984; Taylor and McLennan, 1985; Isley, 1995; Isley and Abbott, 1999; Hawkeworth and Kemp, 2006; Herzberg et al., 2010; Dhuime et al., 2015; Korenaga et al., 2017), abiotic silicon isotope fractionation mechanisms recognized today almost certainly existed since the establishment of a hydrologic cycle in the Hadean (Valley et al., 2002). Archean bedrock samples possess ^{30}Si-enriched silicon isotope signatures (Figure 9A, B; this study; Deng et al. (2020), André et al. (2020)) that differ from Archean volcanic rocks, which possess whole rock isotope values near zero per mil (Abraham et al., 2011; Brengman et al., *in press*). The geochemical stability of quartz during chemical weathering (e.g., Nesbitt et al., 1997) means that detrital quartz should be

transferred to the sedimentary record via mechanical breakdown and physical transport processes. By contrast, clays generated during feldspar hydrolysis (Nesbitt and Markovics, 1997) should acquire a ^{30}Si-depleted silicon isotope signal that reflects the dissolution-precipitation interactions of their formation (Ziegler et al., 2005). Silicon locked up as quartz and silicate minerals in the form of detrital grains is ultimately delivered to the ocean system as clastic particles and deposited to form detrital sediment packages. These same processes would deliver detrital sediments to the ocean system at other times in Earth history. Chemical weathering of any emergent, granodioritic, continental crust would have generated isotopically heavy ($\delta^{30}Si > 0$) silicic acid to the ocean reservoir. Subsequent dissolved Si (dSi as $H_4SiO_{4(aq)}$ or colloidal SiO_2) produced during chemical weathering would carry a ^{30}Si-enriched signature. There is no expected fractionation during high-temperature hydrothermal alteration, though silicification at lower temperatures may lead to ^{30}Si-enriched signatures of altered precipitates (Brengman et al., in press).

From the BGB, bedrock (gneiss) and sandstone (quartzite) possess ^{30}Si-enriched signatures compared to the modern bulk silicate Earth (Figure 10, areas 1, 2; Savage et al., 2010). Such rocks would broadly represent the isotopic composition of detrital source material to the basin, and the starting composition of crustal materials prior to weathering. The similarity in geochemical trends between Holocene and Precambrian weathering profiles (Nesbitt and Young, 1982; Rainbird et al., 1990) indicates that basic hydrolysis reactions have not changed through geologic time, though rates and intensity could have varied widely (Sleep, 2010). Based on the mature mineralogy of clastic sediments of the shelf succession, terrestrial silicon sources to the BGB system should also include dissolved H_4SiO_4 and colloidal SiO_2 derived from intense chemical weathering of exposed bedrock material, and physically transported solid quartz detritus (Figure 10, area 3). In the BGB system, extreme chemical weathering is evidenced by the pre-metasomatized high chemical index of alteration preserved in fine-grained clastic rocks (Fedo et al., 1996) paired with mineralogically mature quartz arenites. Chemical weathering should have resulted in the preferential incorporation of ^{28}Si into products of chemical weathering (i.e. clays; Ziegler et al., 2005) similar to modern weathering. The resultant dissolved silicon load carried to the basin via riverine systems would have been ^{30}Si enriched to preserve mass balance (Figure 10, area 3). Hydrothermal fluids also likely carried dissolved silica, serving as a secondary source (Figure 10A, area 4). Isotope compositions of Archean volcanic rocks and associated silicified equivalents possess silicon isotope values near 0 to +1 per mil (Van den Boorn et al., 2007; 2010; Abraham et al., 2011; Brengman et al., in press). In modern time, there is no observed fractionation between source rock and hydrothermal fluids (Geilert et al. 2015; Kleine et al., 2018; Mehuet et al., 2007; 2009). Consequently, we expect hydrothermal source fluids to the basin to approximate Archean volcanic rocks. Chert and iron formation would precipitate from this ^{30}Si-enriched reservoir (Figure 10, areas 5 and 6).

7. Conclusions

We measured geochemical and isotopic attributes of several samples that represent sources and sinks to the ~3 Ga Buhwa greenstone belt basin. Overall, we determined that source bedrock (gneiss) and detrital quartz derived from this source have comparable silicon isotope values. Values for both rock types are ^{30}Si-enriched compared to the modern bulk silicate Earth but do overlap with isotopic values measured for Archean rocks of similar composition. This likely indicates that silicon isotope signatures of crustal materials in the Archean were ^{30}Si-

enriched compared to modern. Chert and iron formation from the BGB possess distinct but highly variable silicon isotope signatures, in line with observations made by previous studies. Iron formation is generally ^{30}Si-depleted compared to cherts, likely because of kinetic isotope fractionation during adsorption in the presence of a carrier phase such as aluminum or iron. Isotopic variability in samples from the BGB is not easily attributed to basinal position. Instead, variability could link to local isotope changes in the reservoir, where rapid precipitation of ^{30}Si-depleted material (like quartz in iron formation), would result in an opposite shift in the composition of the reservoir, which would become ^{30}Si-enriched to preserve mass balance. Cherts which possess ^{30}Si-enriched values might precipitate from this isotopically heavy reservoir. Overall, the extreme isotopic variability between individual chert and iron formation samples from the BGB indicates the potential to preserve local isotopic signatures. Taking stratigraphic context and textural data into careful consideration, it may be possible to interpret broad trends in the compiled silicon isotope archive to identify variations in silica concentration in the Precambrian ocean. Such variation may fundamentally link to the emergence and weathering of continental crust and the waning of hydrothermal silica inputs to the oceans across time.

Data Availability

All data for the present study are available in Tables 1-3, and Supplementary Tables S1-S4, to be published upon acceptance of the manuscript.

Acknowledgments

This work was funded by NASA grant EXOB08-0063 awarded to C.M. Fedo, and student research grants awarded to L.A. Brengman from ExxonMobil, the Geological Society of America, the Sedimentary Division of GSA, and the Department of Earth and Planetary Sciences at the University of Tennessee. The University of Minnesota – Duluth provided additional funding for for L.A. Brengman. N. Banerjee acknowledges research funding from NSERC and CFI. The NordSIMS facility is a joint Swedish-Icelandic infrastructure operated under Swedish Research Council grant 2014-06375, contribution ####.

Author contributions

L.A. Brengman and C.M. Fedo planned the research. C.M. Fedo collected samples and performed field work. L.A. Brengman, C.M. Fedo, and M. Whitehouse and performed silicon isotope analyses using SIMS. I. Jabeen and L.A. Brengman completed IRMS analyses in the lab directed by N.R. Banerjee at Western University. L.A. Brengman and C.M. Fedo interpreted the data with input by M.J. Whitehouse, N. Banerjee, and I. Jabeen. L.A. Brengman and C.M. Fedo wrote the paper with input from M.J. Whitehouse, N.R. Banerjee, and I. Jabeen.

List of References

1. Abraham, K., Hofmann, A., Foley, S.F., Cardinal, D., Harris, C., Barth, M.G., André, L. Coupled silicon-oxygen isotope fractionation traces Archean silicification. Earth and Planetary Science Letters 301, 222-230 (2011).

2. Allègre, C. J., and Rousseau, D. The growth of continents through geological time studied by Nd isotope analysis of shales. Earth Planetary Science Letters 67, 19-34 (1984).

3. André, L., Cardinal, D., Alleman, L.Y., Moorbath, S. Silicon isotopes in ∼3.8 Ga West Greenland rocks as clues to the Eoarchaean supracrustal Si cycle. Earth and Planetary Science Letters 245, 162-173 (2006).

4. Barton, J.M. and van Reenen, D.D. When was the Limpopo Orogeny? Precambrian Res., 55: 7-16 (1992).

5. Boggs, S. Principles of Sedimentology and Stratigraphy, 3rd edition, Prentice Hall, 726 p. (2001).

6. Bohlar, R., Kamber, B.S., Moorbath, S., Fedo, C.M., Whitehouse, M.J. Characterisation of early Archaean chemical sediments by trace element signatures. Earth and Planetary Science Letters 222: 43-60 (2004).

7. Brengman, L.A., Fedo, C. M., Whitehouse, M. J., Banerjee, N. R., & Jabeen, I. Textural, geochemical, and isotopic data from silicified rocks and associated chemical sedimentary rocks in the ∼2.7 Ga Abitibi greenstone belt, Canada: insight into the role of silicification, Precambrian Research (2020), doi: https://doi.org/10.1016/j.precamres.2020.105946.

8. Brengman, L.A., Fedo, C.M., Development of a mixed seawater-hydrothermal fluid geochemical signature during alteration of volcanic rocks in the Archean (∼2.7 Ga) Abitibi Greenstone Belt, Canada. Geochimica et Cosmochimica Acta, 227, 227-245 (2018).

9. Brengman, L.A. Distinguishing primary versus secondary geochemical and silicon isotope characteristics of Precambrian chert and iron formation PhD diss., University of Tennessee (2015).

10. Brengman, L.A., Fedo, C. M., and Whitehouse, M. J. Micro-scale silicon isotope heterogeneity observed in hydrothermal quartz precipitates from the> 3.7 Ga Isua Greenstone Belt, SW Greenland. Terra Nova 28.1, 70-75 (2016).

11. Chakrabarti, R., Knoll, A. H., Jacobsen, S. B., Fischer, W. W. Si isotope variability in Proterozoic cherts. Geochimica et Cosmochimica Acta 91, 187-201 (2012).

12. Chown, E. H., N'dah, E., Mueller, W. U., 2000. The relation between iron-formation and low temperature hydrothermal alteration in an Archean volcanic environment. Precambrian Research 101, 263-275.

13. Danielson, A., Mo¨ller, P., Dulski, P. The europium anomalies in banded iron formations and the thermal history of the oceanic crust, Chemical Geology 97: 89– 100 (1992).
14. De la Rocha, C.L., Brzezinkski, M.A., DeNiro, M.J. A first look at the distribution of the stable isotopes of silicon in natural waters. Geochimica et Cosmochimica Acta 64, 2467-2477 (2000).

15. Delstanche, S., Opfergelt, S., Cardinal D., Elsass, F., André L., Delvaux, B. Silicon isotopic fractionation during adsorption of aqueous monosilicic acid onto iron oxide. Geochimica et Cosmochimica Acta 73, 923–934 (2009).

16. Delvigne, C., Cardinal, D., Hofmann, André L. Stratigraphic changes of Ge/Si, REE + Y and silicon isotopes as insights into the deposition of a Mesoarchean banded iron formation. Earth and Planetary Science Letters 355-356, 109-118 (2012).

17. Dhuime, B., Wuestefeld, A., Hawkesworth, C.J. Emergence of continental crust about 3 billion years ago. Nature Geoscience 8, 552–555 (2015).

18. Ding, T. Silicon isotope geochemistry, Geological Publishing house, pp. 1-105 (1996).

19. Dodson, M.H., Compston, W., Williams, I.S., Wilson, J.F., 1988. A search for ancient zircons in Zimbabwean sediments. Journal of the Geological Society London 145, 977 983.

20. Fedo, C. M., Eriksson, K. A., and Blenkinsop, T.G., 1995. Geologic history of the Archean Buhwa Greenstone Belt and surrounding granite-gneiss terrane, Zimbabwe, with implications for the evolution of the Limpopo Belt. Canadian Journal of Earth Sciences 32, 1977-1990.

21. Fedo C. M., Eriksson K. A., 1996. Stratigraphic framework of the ~ 3.0 Ga Buhwa Greenstone Belt: a unique stable-shelf succession in the Zimbabwe Archean Craton. Precambrian Research 77, 161-178.

22. Fedo, C., Eriksson, K., Krogstad, E. Geochemistry of shales from the Archean (~3.0 ga) Buhwa Greenstone Belt, Zimbabwe: Implications for provenance and source-area weathering. Geochimica et Cosmochimica Acta, 60 (10): 1751 – 1763 (1996).

23. Frei, R., Polat A. Source heterogeneity for the major components of similar to 3.7 Ga Banded Iron Formations (Isua Greenstone Belt, Western Greenland): tracing the nature of interacting water masses in BIF formation. Earth and Planetary Science Letters 253, 266-281 (2007).

24. Geilert, S., Vroon, P.Z., Roerdink, D.L., Van Cappellen, P., van Bergen, M.J. Silicon isotope fractionation during abiotic silica precipitation at low temperatures: Inferences from flow-through experiments. Geochimica et Cosmochimica Acta 142, 95-114 (2014).

25. Geilert, S., Vroon, P.Z., Keller, N.S., Gudbrandsson, S., Stefansson, A., van Bergen, M.J. Silicon isotope fractionation during silica precipitation from hot-spring waters: Evidence from the Geysir geothermal field, Iceland. Geochimica et Cosmochimica Acta, 154, 403-427

(2015).

26. Gourcerol, B., Thurston, P.C., Kontak, D.J., Côté-Mantha, O., Biczok, J. Depositional setting of Algoma-type banded iron formation. Precambrian Research 281, 47–79 (2016).

27. Gross, G.A. A classification of iron-formation based on depositional environments. Canadian Mineralogist 18, 215–222 (1980).

28. Hamade, T., Konhauser, K., Raiswell, R., Goldsmith, S., Morris, R. Using Ge/Si ratios to decouple iron and sil ica fluxes in Precambrian banded iron formations. Geology. 31, 35-38 (2003).

29. Hawkesworth, C.J., Bickle, M.J., Gledhill, A.R., Wilson, J.F. and Orpen, J.L. A 2.9 b.y. event in the Rhodesian Archaean. Earth Planet. Sci. Lett., 43: 285-297 (1979).

30. Hawkesworth, C. J., Kemp, A. I. S. Evolution of the continental crust. Nature 443, 811 – 817 (2006).

31. Heck, P.R., Huberty, J.M., Kita, N.T., Ushikubo, T., Kozdon, R., Valley, J.W. SIMS analyses of silicon and oxygen isotope ratios for quartz from Archean and Paleoproterozoic banded iron formations. Geochimica et Cosmochimica Acta 75, 5879-5891 (2011).

32. Herzberg, C., Condie, K., Korenaga, J. Thermal history of the Earth and its petrological expression. Earth and Planetary Science Letters 292, 79-88 (2010).

33. Hill, P.J.A., Banerjee, N.R., Ali, A., JAbeen, I., Osinski, G.R., Longstaffe, F.J. Coupled Si and O isotope measurements of meteoritic material by laser fluorination isotope ratio mass spectrometry. J. of Mass Spectrometry, 54 (8), 667-675 (2019). https://doi.org/10.1002/jms.4381.

34. Isley, A.E. Hydrothermal plumes and the Delivery of Iron to Banded Iron Formation. The Journal of Geology 103, 169-185 (1995).

35. Isley, A.E., and Abbott, D.H. Plume-related mafic volcanism and the deposition of banded iron formation. J. Geophys. Res. 104, 15461–15477 (1999).

36. Kimberley, M.M., 1979. Geochemical distinctions among environmental types of iron formations. Chemical Geology 25, 185-212 (1979).

37. Klein, C. Some Precambrian banded iron-formations from around the world: their age, geologic setting, mineralogy, metamorphism, geochemistry, and origin. American Mineralogist, 90: 1473 – 1499 (2005).

38. Kleine, B.I., Stefánsson, A., Halldórsson, S.A., Whitehouse, M.J. and Jónasson, K., Silicon and oxygen isotopes unravel quartz formation processes in the Icelandic crust. Geochemical Perspectives Letters 7, 5–11 (2018).

39. Knauth, L.P., Petrogenesis of chert: In Reviews in Mineralogy, 29: 233-256 (1994).

40. Knauth, L.P., Lowe, D.R. High Archean climatic temperature inferred from oxygen isotope geochemistry of cherts in the 3.5 Ga Swaziland Supergroup, South Africa. GSA Bulletin: 115, p. 566-580 (2003).

41. Konhauser, K.O., Planavsky, N.J., Hardisty, D.S., Robbins, L.J., Warchola, T.J., Haugaard, R., Lalonde, S.V., Partin, C.A., Oonk, P.B.H., Tsikos, H., Lyons, T.W., Bekker, A., Johnson, C.M. Iron formations: A global record of Neoarchaean to Paleoproterozoic environmental history. Earth-Science Reviews 172, 140-177 (2017).

42. Korenaga, J., Planavsky, N.J., Evans, D.A.D. Global water cycle and the coevolution of the Earth's interior and surface environment. Phil. Trans. R. Soc. A 375, 20150393 (2017).

43. Maliva, R.G., Knoll, A.H., Simonson, B.M. Secular change in the Precambrian silica cycle: insights from chert petrology. Geol. Soc. Am. Bull. 117, 835–845 (2005).

44. Michard, A., Albare`de, F., The REE content of some hydrothermal fluids, Chemical Geology 55 (1 – 2) 51–60 (1986).

45. Mkweli, S., Kamber, B. and Berger, M. A westward continuation of the Zimbabwe Craton-Northem Marginal Zone tectonic break and new age constraints on timing of the thrusting. J. Geol. Soc. London, 152: 77-83 (1995).

46. Me´heut M., Lazzeri M., Balan E. and Mauri F. (2007) Equilibrium isotopic fractionation in the kaolinite, quartz, water system: prediction from first-principles density-functional theory. Geochim. Cosmochim. Acta 71, 3170–3181.

47. Me´heut M., Lazzeri M., Balan E. and Mauri F. (2009) Structural control over equilibrium silicon and oxygen isotopic fractionation: a first-principles density-functional theory study. Chem. Geol. 258, 28–37.

48. Nesbitt, H.W., and Markovics, G. Weathering of the Toorongo Granodiorite, storage of elements in weathering profiles, and genesis of siliciclastic sediments. Geochimica Cosmochimica Acta 61, 1653-1670 (1997).

49. Nesbitt, H.W., and Young, G.M. Early Proterozoic climates and plate motions inferred from major element chemistry of lutites. Nature 299, 715-717 (1982).

50. Oelze, M., von Blanckenburg, F., Bouchez, J., F., Hoellen, D., Dietzel. The effect of Al on Si isotope fractionation investigated by silica precipitation experiments, Chemical Geology 397, 95-105 (2015).

51. Oelze, M., von Blanckenburg, F., Hoellen, D., Dietzel, M., Bouchez, J. Si stable isotope fractionation during adsorption and the competition between kinetic and equilibrium isotope fractionation: Implications for weathering systems. Chemical Geology 380, 161-171 (2014).

52. Opfergelt, S., Cardinal, D., Andre, L., Delvigne, C., Bremond, L., Delvaux, B. Variations of δ^{30}Si and Ge/Si with weathering and biogenic input in tropical basaltic ash soils under monoculture. Geochimica et Cosmochimica Acta 74, 225-240 (2010).

53. Pecoits, E., Smith, M.L., Catling, D.C., Philippot, P., Kappler, A., Konhauser, K.O. Atmospheric hydrogen peroxide and Eoarchean iron formations. Geobiology 13, 1–14 (2015).

54. Perry, E.C., Tan, F.C., Morey, G.B. Geology and Stable Isotope Geochemistry of the Biwabik Iron Formation, Northern Minnesota. Economic Geology, 68: 1110-1125 (1973).

55. Rainbird, R.H., Nesbitt, H.W., Donaldson, J.A. Formation and Diagenesis of a Sub-Huronian Saprolith: Comparison with a Modern Weathering Profile. The Journal of Geology 98 (1990).

56. Robert, F., Chaussidon, M., 2006. A paleotemperature curve for the Precambrian oceans based on silicon isotopes in chert. Nature 443: 969-972.

57. Savage, P.S., Georg, R.B., Armytage, R.M.G., Williams, H.M., Halliday, A.N. Silicon isotope homogeneity in the mantle. Earth and Planetary Science Letters 295, 139-146 (2010).

58. Siever, R. The silica cycle in the Precambrian. Geochimica et Cosmochimica Acta 56, 3265-3272 (1992).

59. Sleep, N.H. The Hadean-Archaean Environment. Cold Spring Harb Perspect Biol. 2 (6): a002527 (2010).

60. Stamm, F., Mehuet, M., Zambardi, T., Chmeleff, J., Schotta, J., Oelkers, E. Extreme silicon isotope fractionation due to Si organic complexation: Implications for silica biomineralization. Earth and Planetary Science Letters 541: 116 – 287 (2020).

61. Stefurak, E.J.T., Fischer, W.W. and Lowe, D.R. Texture-specific Si isotope variations in Barberton Greenstone Belt cherts record low temperature fractionations in early Archean seawater. Geochim. Cosmochim. Acta 150, 26–52 (2015).

62. Tatzel, M., Blanckenburg, F., Oelze, M., Schuessler, J., Bohrmannc, G. The silicon isotope record of early silica diagenesis. Earth and Planetary Science Letters 428 (2015) 293–303 (2015).

63. Taylor, S.R., McLennan, S.M. The Continental Crust: its Composition and its Evolution, Blackwell, Oxford, 312 pp. (1985).

64. Treguer, P.J., De La Rocha, C.L. The World Ocean Silica Cycle, Annu. Rev. Mar. Sci. 5, 477-501 (2013).

65. Valley, J.W., Peck, W.H., King, E.M., Wilde, S.A. A cool early Earth. Geology 30, 351-354 (2002).

66. Van den Boorn, S. H. J. M., van Bergen, M. J., Nijman, W., Vroon, P. Z. Dual Role of seawater and hydrothermal fluids in Early Archean chert formation: Evidence from silicon isotopes. Geology 35, 939-942 (2007).

67. Van den Boorn, S.H.J.M., van Bergen, M.J., Vroon, P., de Vries, S.T., Nijman, W. Silicon isotope and trace element constraints on the origin of ~3.5 Ga cherts: Implications for Early Archaean marine environments. Geochimica et Cosmochimica Acta 74, 1077-1103 (2010).

68. Wilson, J.F., Jones, D.L. and Kramers, J.D. Mafic dyke swarms in Zimbabwe. In: H.C. Halls and W.F. Fahrig (Editors), Geol. Assoc. Can. Spec. Pap., 34: 433-444 (1987).

69. Wilson, J.F. A craton and its cracks: some of the behavior of the Zimbabwe block from the Late Archean to the Mesozoic in response to horizontal movements, and the significance of some of its mafic dyke fracture patterns. Journal of African Earth Sciences (and the Middle East) 10, 483-501 (1990).

70. Worst, B.G. The geology of the Buhwa iron ore deposits and adjoining country: Belingwe district. S. Rhodesia Geol. Surv., 53, 114 pp (1962).

71. Zheng, X., Beard, B., Johnson, C. Constraining silicon isotope exchange kinetics and fractionation between aqueous and amorphous Si at room temperature. Geochimica et Cosmochimica Acta, 267-289 (2019).

72. Ziegler, K., Chadwick, O. A., White, A. F., Brzezinski, M. A. d30Si systematics in a granitic saprolite, Puerto Rico. Geology 33, 817-820 (2005).

73. Ziegler, K., Dodd, J.P., Sharp, Z.D., Brearley, A.J., Young, E.D., 2011. Silicon and oxy-gen isotope values of cherts and their precursors. In: Goldschmidt Conference Abstracts, p.2284 (2011).

FIGURES for draft manuscript *"Evaluating the geochemistry and paired silicon and oxygen isotope record of quartz in siliceous rocks from the ~3 Ga Buhwa Greenstone Belt, Zimbabwe, a critical link to deciphering the Archean silica cycle"*

Latisha A. Brengman[1, 2]*, Christopher M. Fedo[1], Martin J. Whitehouse[3], Iffat Jabeen[4], Neil R. Banerjee[4]

[1]Department of Earth and Planetary Sciences, University of Tennessee, Knoxville, TN 37996, USA, [2]Department of Earth and Environmental Sciences, University of Minnesota – Duluth, Duluth, MN, 55812 USA, [3]Department of Geosciences, Swedish Museum of Natural History, Stockholm, Sweden, SE-105 05, [4]Department of Earth Sciences, Western University, London, Ontario, Canada, N6A 5B7

Corresponding Author*: Latisha A. Brengman, Department of Earth and Environmental Sciences, University of Minnesota – Duluth, 1114 Kirby Drive, 221 Heller Hall, Duluth, MN, 55812, Phone: (218)-726-7586, Email: lbrengma@d.umn.edu

Keywords: silicon isotopes, oxygen isotopes, Mesoarchean silica cycle, Superior-type iron formation, Algoma-type iron formation, chert, geochemistry, source to sink

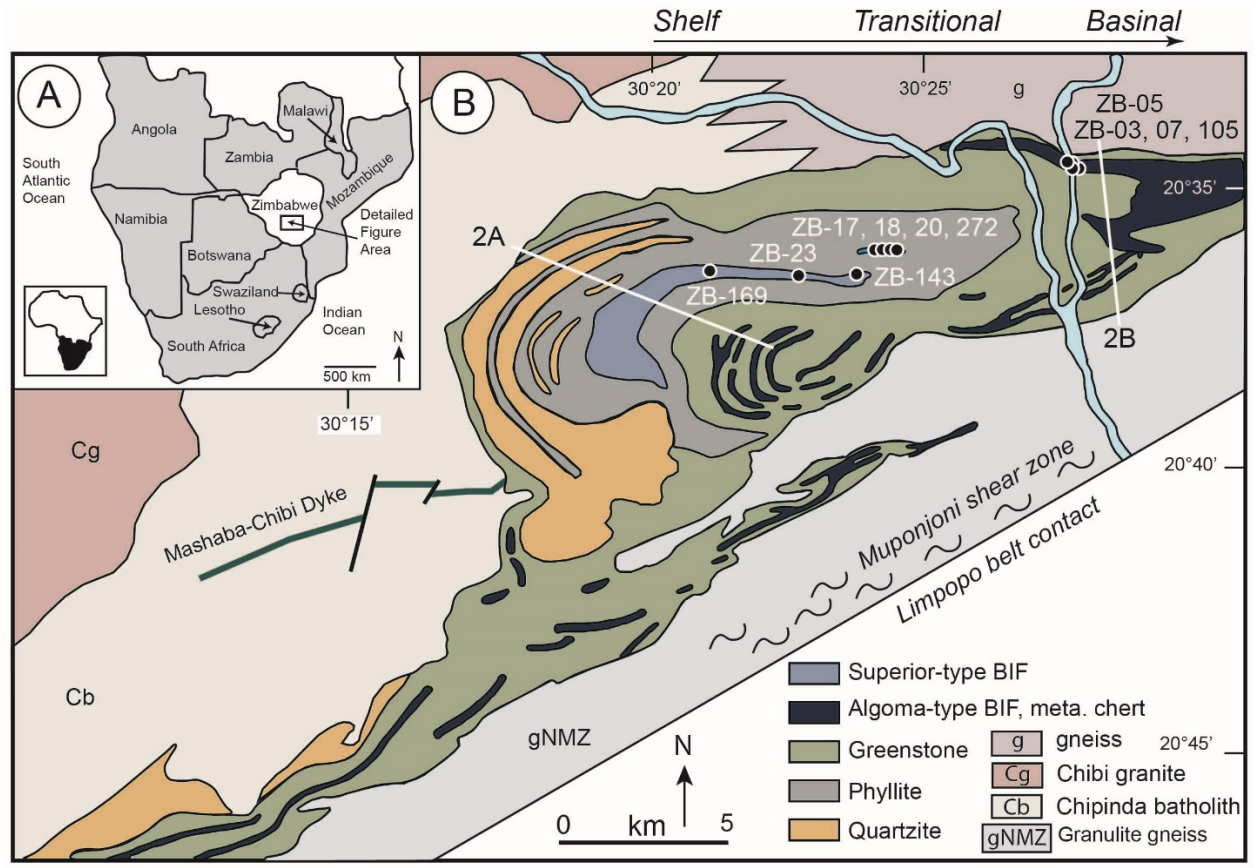

Figure 1. Geologic map of the ~3 Ga Buhwa greenstone belt, Zimbabwe, based on Fedo et al., (1995), (1996), and Fedo and Eriksson, (1996). (A) Geographic location of the Buhwa greenstone belt. (B) Geologic map of the Buhwa greenstone belt with stratigraphic column locations (2A – shelf association, 2B, basinal association), generalized sample locations, and major rock types.

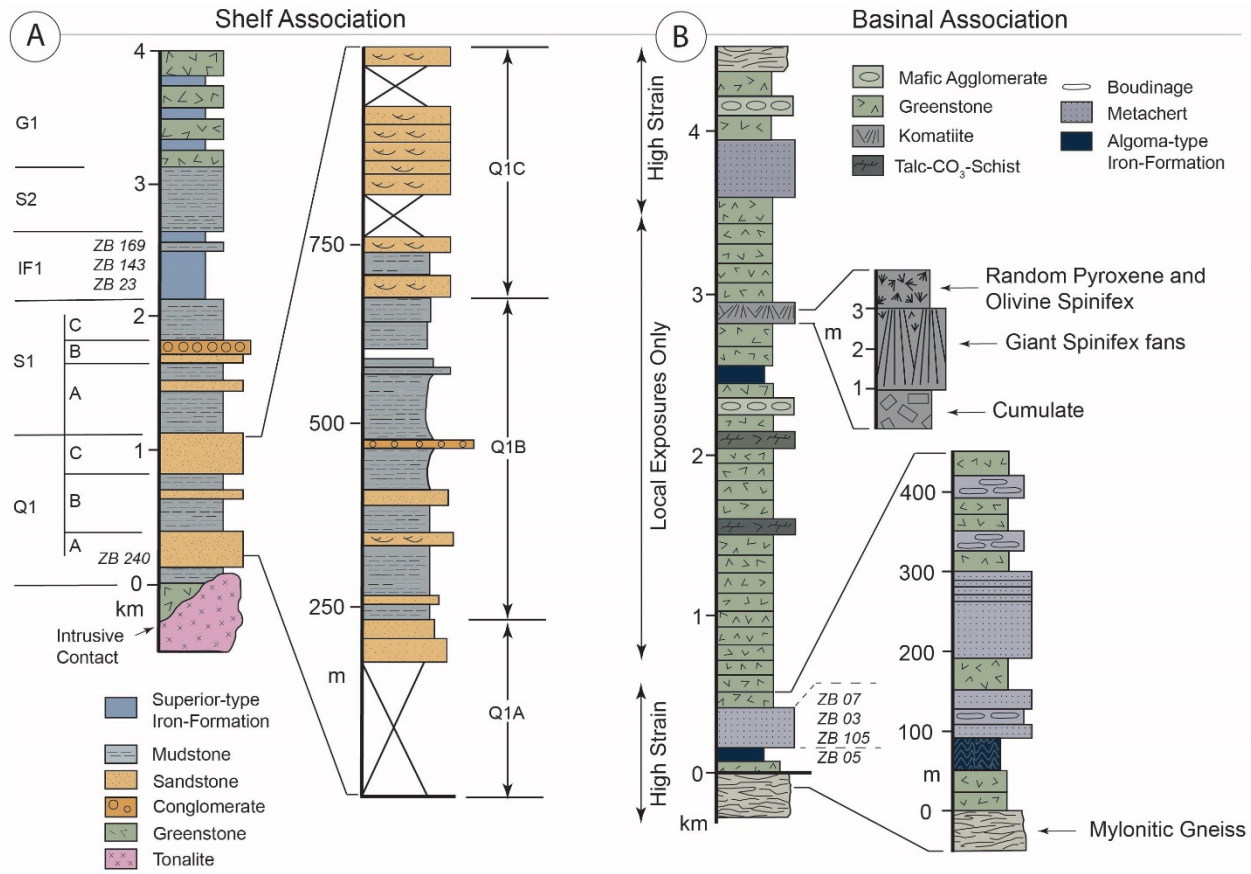

Figure 2. Stratigraphic columns of the shelf association and basinal association within the Buhwa greenstone belt adapted from Fedo and Eriksson, (1996). (A) Stratigraphic column of the shelf association – note preservation of sedimentary structures. Samples include ZB 240 (quartzite), and ZB 23, 143, and 169 (Superior-type iron formation). (B) Stratigraphic column of the basinal association. Samples include ZB 03, 07, and 105 (chert), and ZB 05 (Algoma-type iron formation). Note the difference in associated rock types for each iron formation sample set.

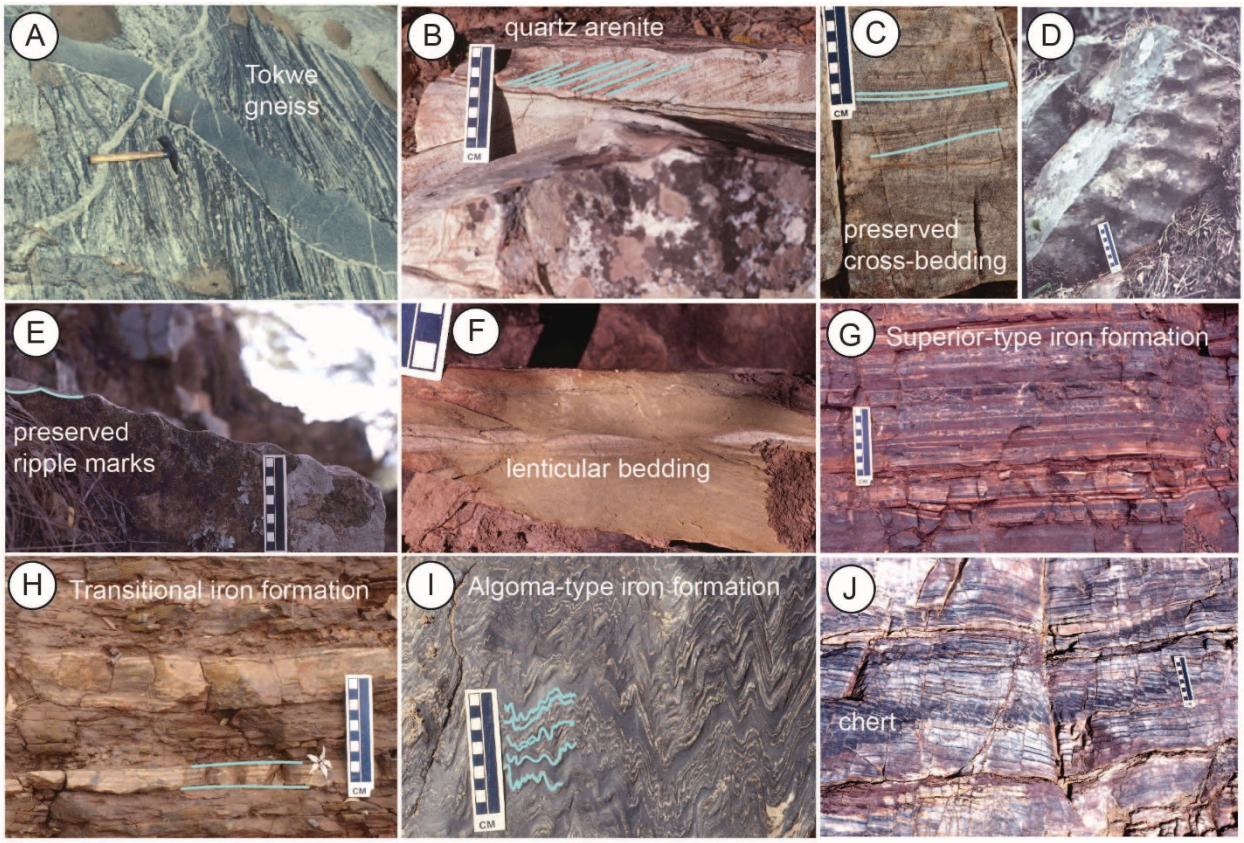

Figure 3. Field photographs of important features from the shelf, transitional, and basinal associations in the BGB. Alternating dark and light boxes on the scale card each represent one centimeter. (A) Tokwe gneiss source material with inclusions of BGB quartzite. Large hammer for scale. (B, C) Cross-bedding and symmetrical ripple-marks (D, E) preserved in the quartzite unit of the shelf association. (F) Lenticular bedding preserved in mud-rich units of the shelf association. (G) Superior-type iron formation of the shelf association consisting of quartz, hematite, magnetite. (H) Iron formation from the transitional association. (I) Deformed Algoma-type iron formation of the basinal association. Mineralogy includes quartz, magnetite, and minor amounts of amphibole. (J) Chert interbedded with Algoma-type iron formation of the basinal association. Banding relates to compositional differences between layers, which alternate between quartz and minor amounts of organic material (now graphite). Note the offset of layers.

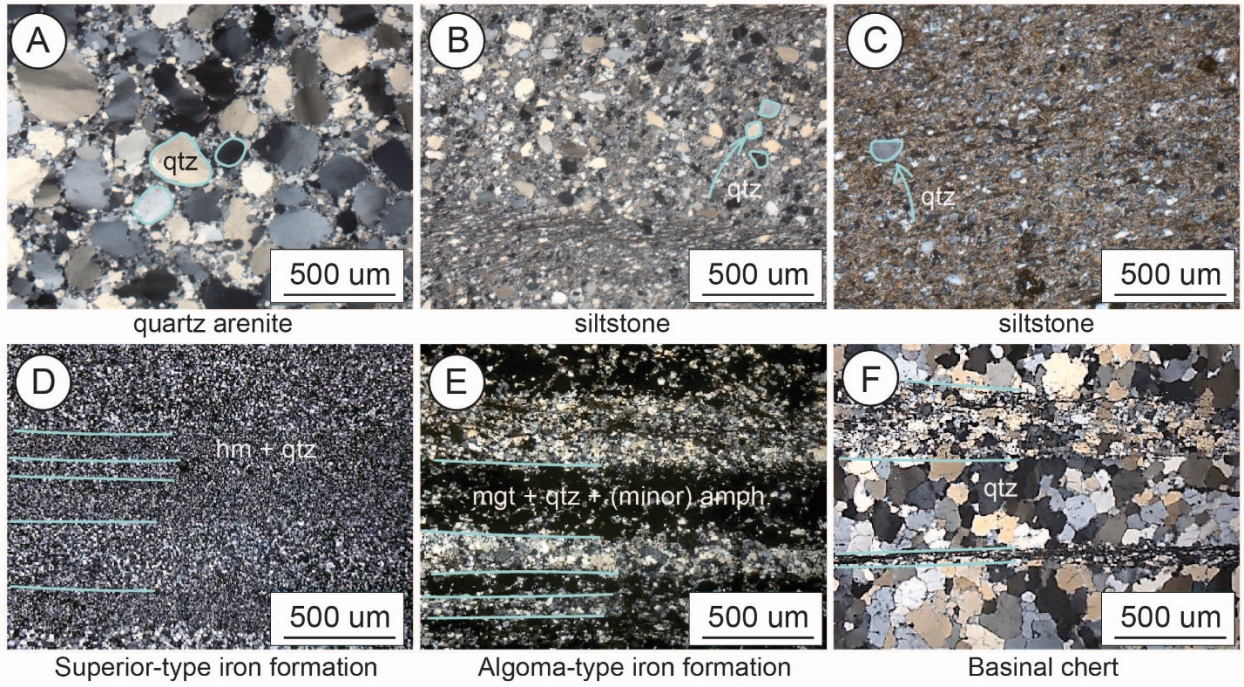

Figure 4. Cross-polarized light photomicrographs of select samples. (A) Rounded, medium-sized sand grains preserved in quartz-cemented quartz arenite (now quartzite) of the shelf association. (B) Detrital quartz silt preserved in mud-rich units of the shelf association. (C) Detrital quartz silt preserved in shale (now phyllite). (D) Superior-type iron formation of the shelf association. Mineralogy includes alternating layers of quartz, and quartz + hematite with minor amounts of magnetite. (E) Algoma-type iron formation of the basinal association. Layers defined by different proportions of iron-oxides. Mineralogy includes quartz, magnetite, and minor amounts of amphibole. (F) Chert associated with Algoma-type iron formation of the basinal association. Layers defined by minor amounts of organic material (now graphite).

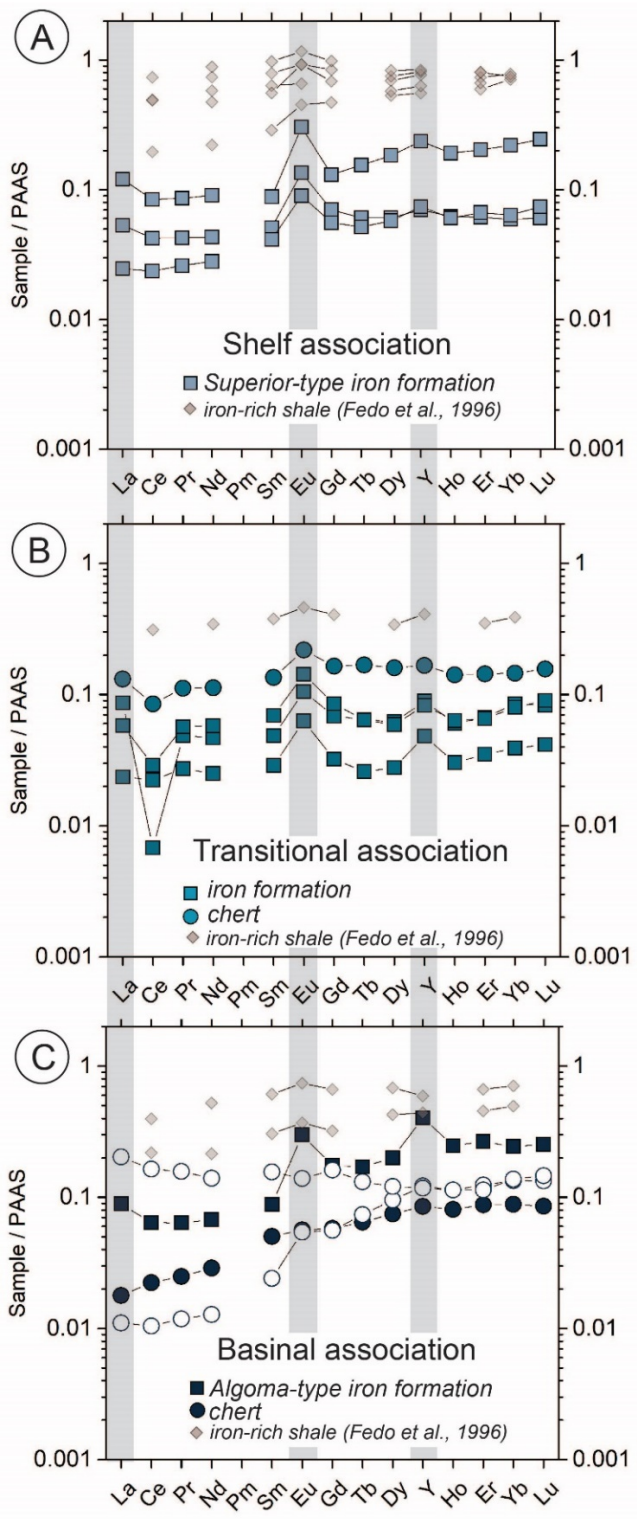

Figure 5. Rare earth element and yttrium data for iron formation and chert samples from the shelf (A), transitional (B), and basinal (C) associations of the BGB. All data is normalized to PAAS. Shale geochemical data from each association from Fedo et al., 1996 is plotted for comparison.

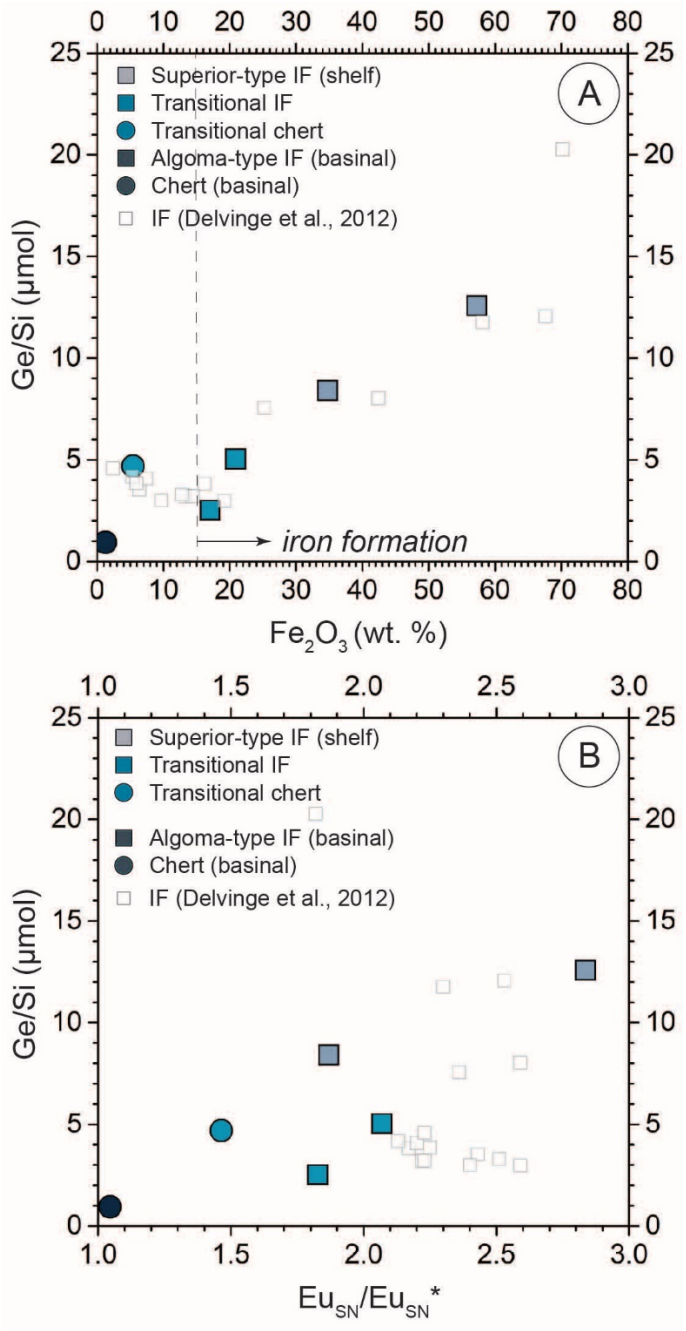

Figure 6. Select geochemical data for samples from the BGB. Samples are grouped by rock type into Superior-type iron formation from the shelf association, transitional iron formation and chert, and Algoma-type iron formation and chert from the basinal association. (A) Ge/Si versus silicon isotope value (A), iron contents (B), and europium anomaly (Eu/Eu_{SN}*; C) for samples from the BGB compared to Archean iron formation samples from Delvigne et al. (2012). Iron formation are defined as having > 15% Fe content. There is a weak correlation between Ge/Si and both iron content and europium anomaly.

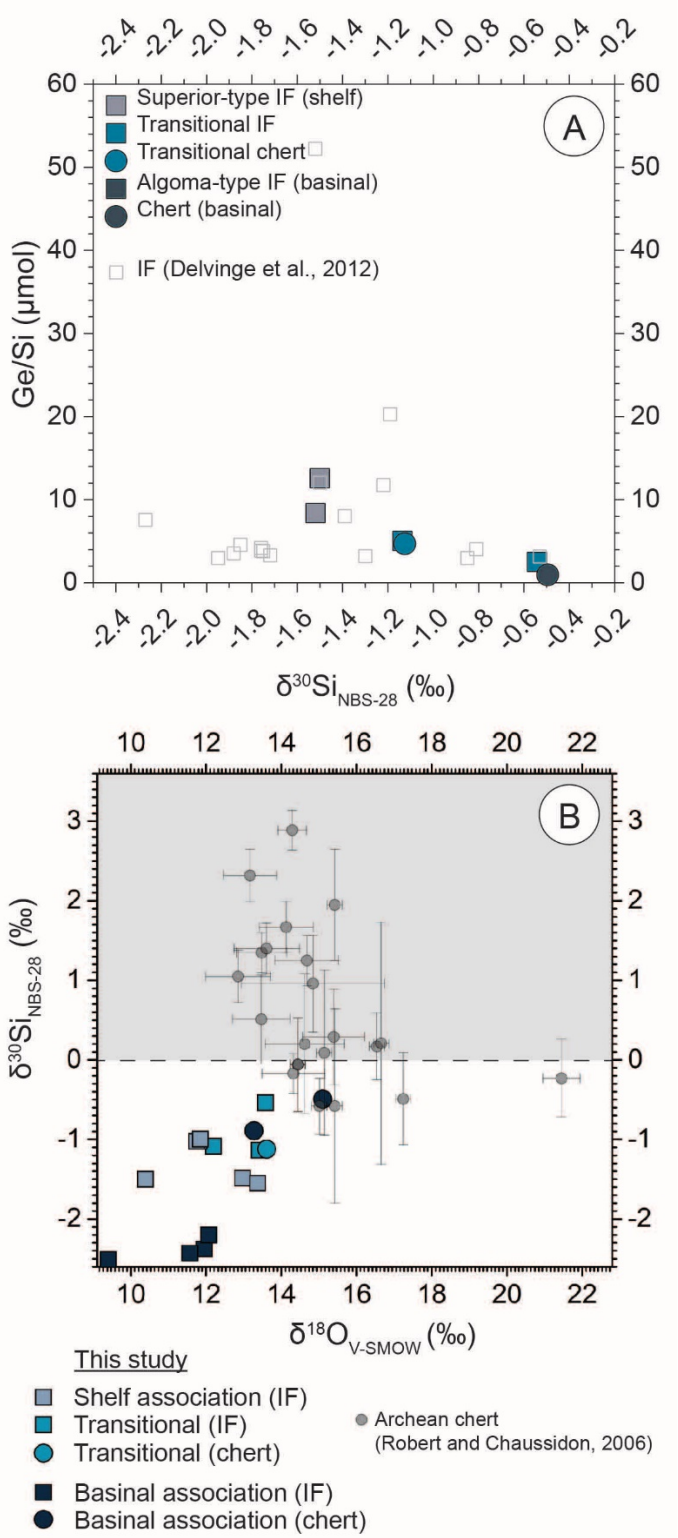

Figure 7. Multi-crystal silicon and oxygen isotope data obtained via IRMS for samples from this study compared to Archean chert samples from Robert and Chaussidon, (2006). Samples are separated by rock type and association within the BGB. Error is smaller than the symbol size (0.03 per mil) for samples from the BGB.

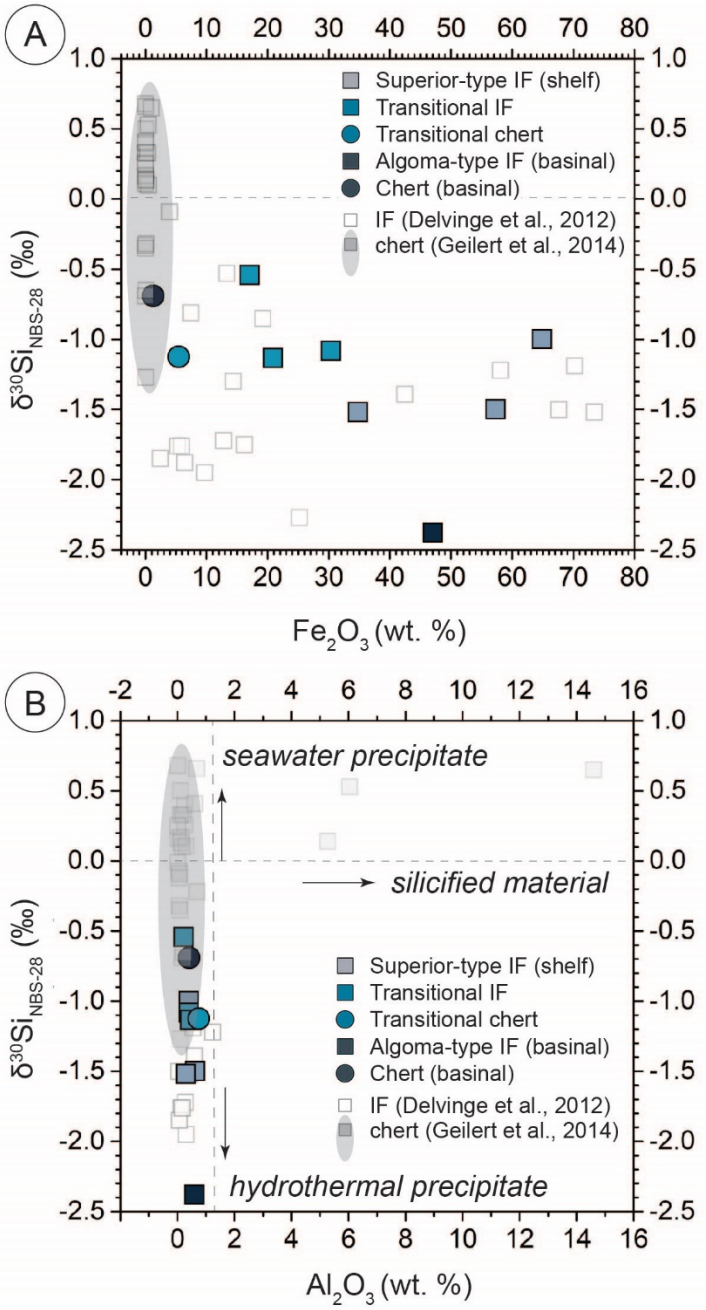

Figure 8. Multi-crystal silicon isotope data obtained via IRMS for samples from the present study plotted against aluminum and iron contents. Comparable Archean iron formation and chert samples from Delvinge et al. (2012) and Geilert et al. (2014) are plotted for visual comparison. (A) Silicon isotope values versus iron content for BGB samples are separated by rock type and association within the basin. There is a notable difference between chert and iron formation isotope compositions. (B) Silicon isotope values versus alumni content for the same samples plotted in A. Labels of seawater precipitate, silicified material, and hydrothermal precipitate are after Geilert et al. (2014).

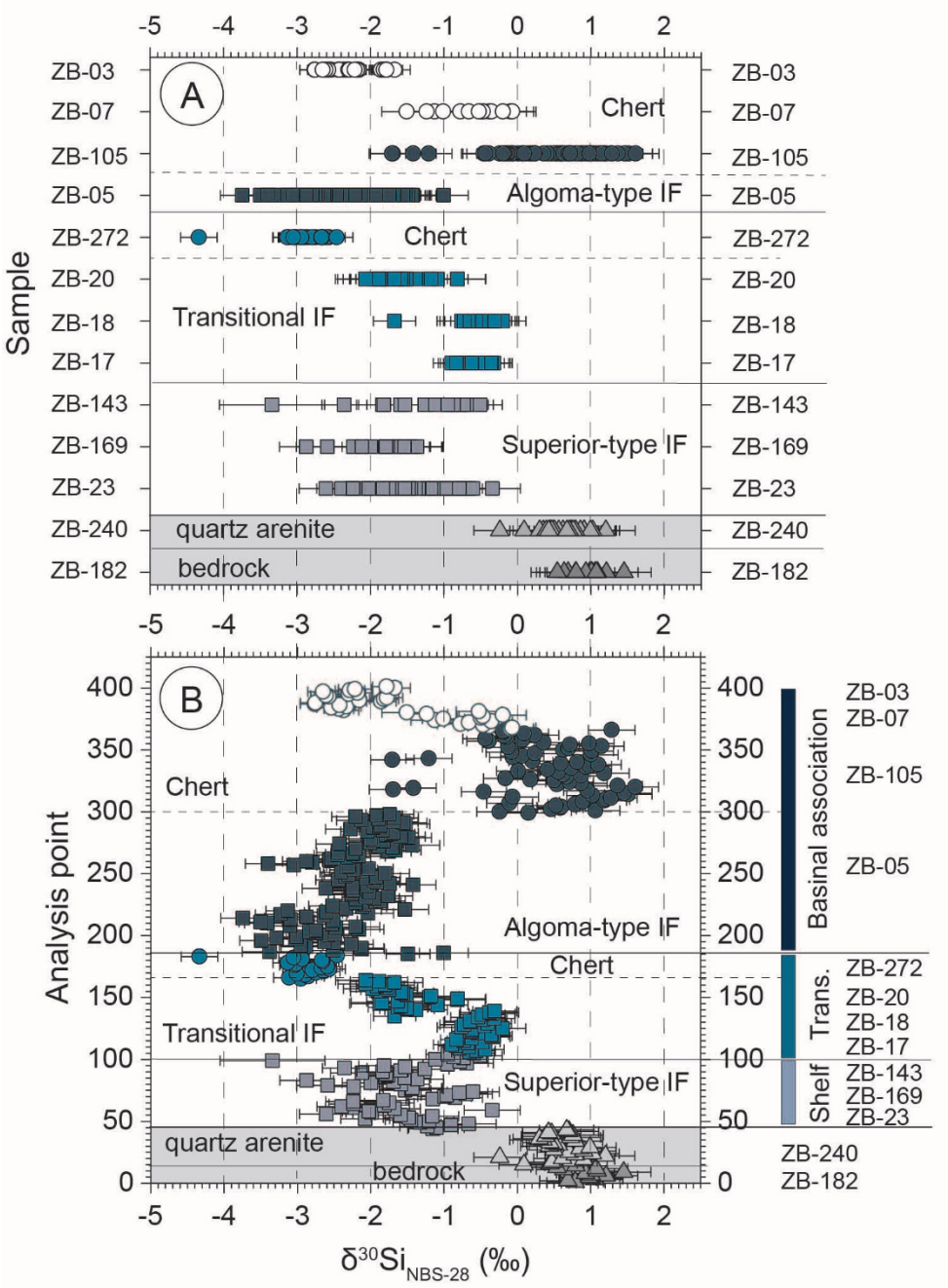

Figure 9. Single-crystal silicon isotope data obtained via SIMS for samples from the BGB. (A) Silicon isotope values are grouped by sample. (B) Samples are separated by association, and individual point analyses.

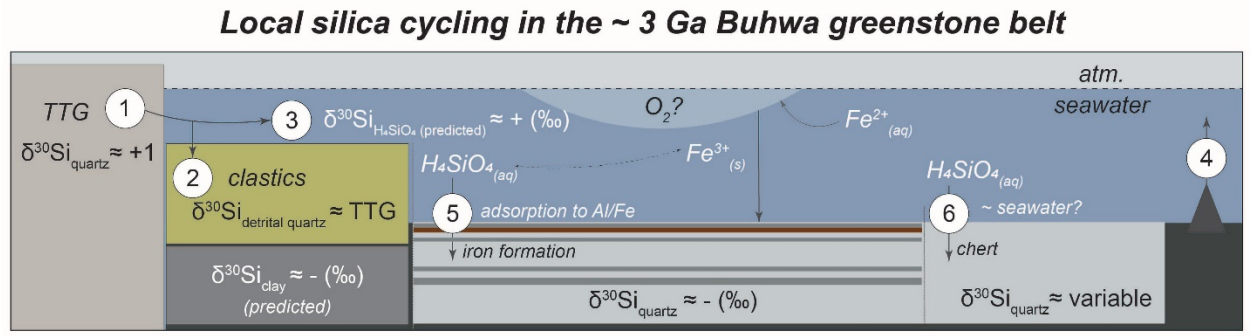

Figure 10. Schematic diagram for the balance of the Mesoarchean silica cycle based on data from the Buhwa greenstone belt. Diagram follows silica from source (bedrock) to sink (Superior-type and Algoma-type iron formation, and chert) in the BGB. Measured values for detrital quartz, quartz in bedrock, quartz in iron formation, and quartz in chert are labeled with their generalized signature (- indicating ^{30}Si-depleted, and + indicating ^{30}Si-enriched). Positive and negative symbols within boxes over generalized reservoirs correspond to ^{30}Si-enrichement or depletion respectively. Seafloor silicification is noted in many other Archean assemblages, and though it is not of note in the BGB, it is included in the overall balance of the silica cycle. Numbers correspond to the in-text description.